CrossMark

Synthesis of triphasic, biphasic, and monophasic TiO$_2$ nanocrystals and their photocatalytic degradation mechanisms

Shujie Wang[1] · **Huiling Yu**[1] · **Shuai Yuan**[1] ·
Yin Zhao[1] · **Zhuyi Wang**[1] · **Jianhui Fang**[1] ·
Meihong Zhang[1] · **Liyi Shi**[1]

Abstract The preparation of the triphasic (anatase/rutile/brookite), biphasic (anatase/brookite), and monophasic (anatase) TiO$_2$ nanocrystals from peroxotitanium complex (PTC) as precursor by the hydrothermal method was reported in this work. The experimental results indicated that a large window for tuning the phase compositions was achieved by varying the HCl/PTC ratio due to the high stability of PTC. Moreover, the growth mechanism and microstructure evolution of the obtained TiO$_2$ nanocrystals were discussed. The liquid-phase photocatalytic degradation of phenol under UV illumination was used as a model reaction to evaluate the photocatalytic activity of the synthesized materials. The photocatalytic activity is as follows: anatase/brookite biphase > anatase monophase > anatase/rutile/brookite triphase TiO$_2$ nanocrystals. The possible photodegradation mechanism was studied by the examination of active species such as ·OH, photogenerated electrons and holes through adding their scavengers such as methanol, t-BuOH, and K$_2$S$_2$O$_8$. Although the anatase/rutile/brookite triphase TiO$_2$ nanocrystals samples show the most effective separation ability of photo-induced electron–hole pairs, the anatase/brookite biphase TiO$_2$ nanocrystals samples exhibited the highest photocatalytic activity, which can be attributed to effective formation of the activated radicals.

✉ Yin Zhao
zhaoyin@shu.edu.cn

✉ Liyi Shi
shiliyi@shu.edu.cn

[1] Research Center of Nanoscience and Nanotechnology, Shanghai University, 99 Shangda Road, Shanghai 200444, People's Republic of China

🍀 Springer

Introduction

Semiconductor-mediated photocatalytic oxidation and reduction potentially offer a simple and cheap method for removing harmful compounds in environment [1]. Among various oxide semiconductor photocatalysts, titanium dioxide is one of the most suitable catalysts because of its relatively high photocatalytic activity, chemical stability, nontoxicity, and low cost [2]. However, a major obstacle for the practical application of titania is its fast recombination rate of photogenerated electron/hole pairs, which leads to low quantum efficiency [3].

Currently, intense research has been focused on coupling semiconductors possessing different redox energy levels for their corresponding conduction and valence bands, which has been proved to be an efficient way to increase the charge separation rate and the lifetime of charge carriers [4]. For example, TiO$_2$ with mixed anatase and rutile phase shows enhanced photocatalytic activity [5–7]. Moreover, the high photoactivity of Degussa P25, that is frequently used as a benchmark in heterogeneous photocatalysis, correlates to the existence of a mixture of anatase and rutile phases [8]. Evidently, the coupling of different phases TiO$_2$ can be proposed as a strategy for enhancing the charge separation to reduce electron–hole recombination [9].

In addition to anatase and rutile, TiO$_2$ can form the brookite phase, which has been least studied in many aspects of its properties due to the difficulty in synthesis. Recently, Vargeese et al. [10] reported that the anatase–brookite composite TiO$_2$ nanocrystals showed much higher photocatalytic activity than that of anatase. Gai et al. [11] reported that TiO$_2$ photocatalyst with biphase of brookite and anatase showed higher photocatalytic activity than Degussa P25. But Boppella et al. [12] presented some evidence that samples containing anatase and a large amount of brookite were less active than pure anatase for the photodecomposition of RhB. Moreover, the effective single heterojunction system drives exploring the effect of the multiheterojunction on photoelectrochemical behaviors. Liao et al. [13] prepared brookite/anatase/rutile coexisting TiO$_2$ with higher photocatalytic activities rather than single phase and binary phase nanocomposites. However, Zhang et al. [14] presented some evidence that samples containing anatase, brookite, and rutile phase were less active than biphase samples for the photodecomposition of a solution of methylene blue. These contrasting results arouse an effort aiming to obtain deeper insight into the photoactivity mechanism of mixed phase TiO$_2$.

Especially, the operation of a multiheterojunction is different from a single heterojunction, in which at least three layers of different semiconductors meet at one interface [15]. For example, Wu et al. [16] prepared the n-CdS/n-TiO$_2$/p-BDD triple heterojunction. They found that this triple heterojunction CdS hybrid shows 36.5 % improvement of initial photocurrent and 78 % reduction of photocorrosion rate in contrast with that of the coupled CdS/TiO$_2$ hybrid, which has only single heterojunctions (SH). Nowadays, several studies focus on the improvement of the

photocatalytic activity by controlling the phase ratio of mixed phase TiO_2 [12]. However, little is known about the photoactivity mechanism of the mixed phase TiO_2. Moreover, the through studies of the mixed phase TiO_2 catalytic behavior in relation not only to the crystalline phase, but also to the intermediate radical species may be a great aid in the design and preparation of efficient semiconductor based photocatalysts.

Herein, anatase, anatase/brookite, and anatase/brookite/rutile mixed phase TiO_2 were prepared by using a facile hydrothermal approach. The growth mechanism and microstructure evolution of mixed phase TiO_2 had been suggested. The liquid-phase photocatalytic degradation of phenol was used as a model reaction to evaluate the photocatalytic activity of the synthesized materials. Based on the experimental results, the mechanistic aspects of phenol photodegradation were elucidated.

Experimental section

Materials and reagents

All the chemicals were used as received without further purification. Titanium (IV) sulfate ($Ti(SO_4)_2$, CR) was obtained from Shanghai Chemical Reagent Co., China. Aqueous ammonia solution (NH_4OH, 25 wt%, AR), aqueous hydrogen peroxide solution (H_2O_2, 30 wt%, AR), absolute ethanol, hydrochloric acid (HCl, 30 wt% AR), and phenol (AR) were purchased from Sinopharm Chemical Reagent Co. Ltd. Deionized water was used for carrying out all the experiments.

Preparation of TiO₂ nanocrystals

Titanium (IV) sulfate ($Ti(SO_4)_2$, CR) was used as Ti source. The 0.125 mol $Ti(SO_4)_2$ was diluted with 125 mL deionized water. The pH value was adjusted to 7.5 by adding 3 M NH_4OH slowly, under vigorous stirring. Simultaneously, the white precipitate was formed. After aging for 12 h, the resulting suspension was filtered and washed. After that, the purified precipitate was diluted with deionized water to attain a total volume of 125 mL. Under continuous stirring, 5 mL H_2O_2 (30 wt%) was slowly added into the suspension. The mixture was stirred for 2 h, and then the peroxotitanium complex (PTC) was formed. After that, the appropriate quantities of hydrochloric acid (2 M) were added dropwise. After refluxed at 95 °C for 4 h, the resulting mixture was transferred to an autoclave, and then was held at 180 °C for 15 h. Finally, the as-prepared TiO_2 nanocrystals were obtained. In the present study, the as-prepared samples have been labeled as TiHx, and x was defined as the molar ratio of HCl–PTC.

Characterization

The as-prepared TiO_2 nanocrystals were prepared through rotatory evaporation of the TiO_2 nanocrystals colloids at 55 °C for the following testing. Powder XRD analysis was carried out using a Rigaku D/MAX-2000 X-ray diffractometer with Cu

K_α radiation ($\alpha = 0.15418$ nm). The crystallite size of the as-prepared samples was determined using the Scherrer equation. The Raman spectra were recorded on an in equipped with an optical micro-scope at room temperature, For excitation, the 514.5 nm line from an Ar^+ ion laser (Spectra Physics) was focused, with an analyzing spot of about 1 mW, on the sample under the microscope. The power of the incident beam on the sample was 1 mW. The time of acquisition was varied according to the intensity of the Raman scattering. Transmission electron microscopy (TEM) information was obtained with a JEOL JEM-200 CX micro-scope electron microscope. The HRTEM images were obtained using a JSM-2010F microscope at an acceleration voltage of 200 kV. The specific surface areas of the samples were determined through nitrogen adsorption at 77 K on the basis of the BET equation (model 3H-2000III, China). Diffuse reflectance spectra (DRS) were obtained for the dry-pressed disk samples using a scanning UV–Vis–NIR spectrophotometer (Varian, Cary 500) equipped with an integrating sphere assembly, using $BaSO_4$ as reflectance sample. The photoluminescence (PL) spectra were measured through a fluorescence spectrophotometer (Hitachi, F-7000) using the 300 nm line of an Xe lamp as an excitation source at room temperature.

Photocatalytic reactions

The photocatalytic activities of the prepared samples were evaluated by measuring the decomposition of 10 mg/L phenol aqueous solution. The UV photocatalytic reactions were carried out in a glass immersion photochemical reactor charged with 70 mL phenol aqueous solution, the concentration of catalyst was 0.1 g/L. Four 8 W low-pressure mercury lamps as UV-light source (wavelength 254 nm), and the irradiation intensity was 0.55 mW/cm^2. All photocatalytic reactions were performed using the identical conditions; 0.07 g of the prepared catalyst was immersed into 70 mL phenol aqueous solution under constant magnetic stirring. After agitated for 30 min to attain the adsorption equilibrium, the samples was taken to test every 30 min during the catalytic process. The sample was analyzed with an UV–Vis spectrophotometer (UV-2501 PC spectrometer). The efficiency of degradation was calculated from the formula (1):

$$\text{Phenol degradation } (\%) = (C_0 - C)/C_0 \times 100\,\% \qquad (1)$$

where C_0 and C are the original phenol concentration after the adsorption/desorption reached equilibrium and residual phenol concentration after reaction.

Results and discussion

Microstructure and optical properties of TiO$_2$ nanocrystals

The XRD patterns of TiO$_2$ nanocrystals samples prepared by different HCl/PTC ratios are provided in Fig. 1. The pattern of sample TiH0 is indexed as the anatase phase of TiO$_2$ (JCPDS file no. 21-1272) [5]. With increasing HCl/PTC ratio, the

Fig. 1 XRD patterns of the TiO$_2$ nanocrystals prepared by different HCl/PTC ratios. *a* TiH0, *b* TiH1, *c* TiH3, *d* TiH10, *e* TiH16. A, B and R represented the anatase, brookite, and rutile phase, respectively
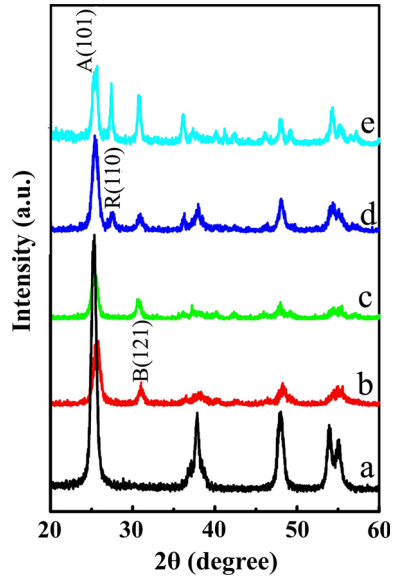
additional diffraction peaks at 30.81° (2θ) corresponding to the brookite phase (JCPDS file no. 29-1360) appear [17]. The anatase and brookite two-phase coexistence with predominance of anatase phase is observed in samples TiH1 and TiH3. Since the typical diffraction from anatase (101) overlaps with the diffraction from brookite (120), the content of brookite phase in the mixture can be estimated by the $I_{brookite(121)}/(I_{brookite(121)} + I_{anatase(101)})$ ratio [18]. Calculation results show that the brookite content increased from 24.8 to 34.8 % corresponding to the sample TiH1–TiH3, respectively (Table 1). Further increasing the HCl/PTC ratio lead to the rutile phase. The sample TiH10 and TiH16 apparently displayed anatase/brookite/rutile triphase coexistence. In the case of triphase coexistence samples, the anatase phase content slightly decreased from 74.8 to 65.8 %, the brookite phase content increased from 17.7 to 27.1 %, and the content of rutile phase was maintained at about 7 %.

Table 1 Characterization of TiO$_2$ nanocrystals prepared by different HCl/PTC ratios

| Sample	Phase detected (%)[a]			Crystallite size (nm)			D_{TEM} (nm)	S_{BET} (m^2/g)	Band gap (E_g)
	A	B	R	D_A	D_B	D_R			
TiH0	100	–	–	12.0	–	–	15.4	107.6	3.24
TiH1	75.2	24.8	–	9.4	11.5	–	14.2	147.6	3.13
TiH3	65.2	34.8	–	10.2	17.5	–	19.7	139.0	3.12
TiH10	74.8	17.7	7.5	10.2	13.6	17.3	22.1	45.1	3.08
TiH16	65.8	27.1	7.1	13.5	25.6	19.0	25.6	65.7	3.10

[a] A, B and R are corresponding to the anantase, brookite, and rutile, respectively

The crystal size for TiO_2 nanocrystal samples prepared by different HCl/PTC ratios was calculated and collected in Table 1. For all samples, the crystal size of the anatase phase showed less variation with the increasing HCl/PTC ratio. In the case of anatase/brookite biphase TiO_2 samples, the brookite crystal size increased from 11.5 to 17.5 nm corresponding to sample TiH1–TiH3, respectively. Furthermore, an obvious increase from 13.6 to 19.0 nm was observed in triphase coexistence TiO_2 samples. These results are in agreement with the previous report that Cl^- ions facilitate the growth of brookite phase by enhanced face-sharing and edge-sharing of TiO_6 octahedra [19]. Moreover, the rutile crystal size for triphase coexistence TiO_2 samples increased from 17.3 to 30.5 nm, which should be attributed to the strong acidic condition and large amount of Cl^- ion promoting the growth of rutile along the [001] direction [20].

The crystal phase evolution of TiO_2 nanocrystals samples prepared by different HCl/PTC ratios were also investigated by Raman spectroscopy. In Fig. 2, only anatase phase peaks at 146, 396, 515, and 641 cm^{-1} were observed in sample TiH0 [21]. With increasing HCl/PTC ratio, there were strong peaks assigned to the anatase phase and additional weak peaks attributed to the brookite phase TiO_2 (153, 247, 322, and 366 cm^{-1}) in sample TiH1 and TiH3 [12], which indicated that the biphase coexistence with predominance of the anatase phase. When the HCl/PTC ratio is further enhanced, besides anatase and brookite phase peaks, the rutile phase peaks at 143, 235, 447, and 612 cm^{-1} appear in sample TiH10 and TiH16 [22]. The Raman results are in good agreement with the XRD analysis results.

Recently, the peroxotitanium complex (PTC) has been reported as a promising intermediate phase for the synthesis of TiO_2 nanocrystals [23–26]. In the present experiment, the result proved that the controllable synthesis of different phases TiO_2 nanocrystal from the PTC precursor by adjusting the HCl/PTC ratio is available. As described in previous literature, PTC is synthesized by the reaction between
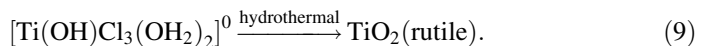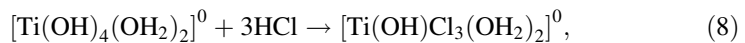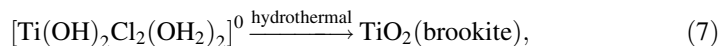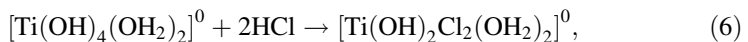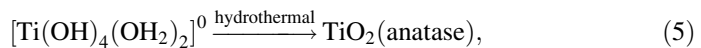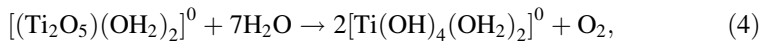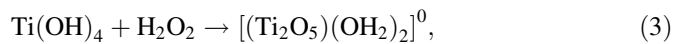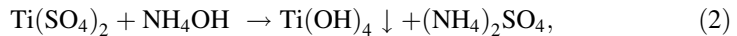

Fig. 2 Raman spectra of TiO_2 nanocrystals. *a* TiH0, *b* TiH1, *c* TiH3, *d* TiH10, *e* TiH16. A, B, and R represented the anatase, brookite, and rutile, respectively
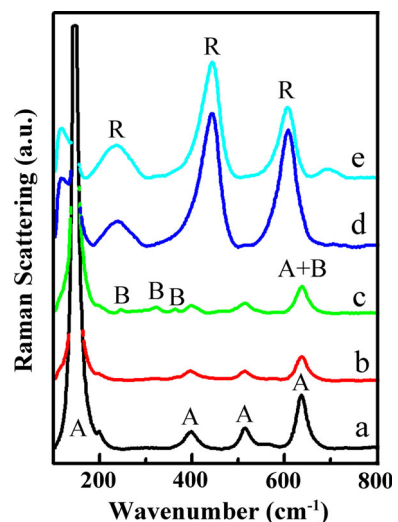
hydrogen peroxide and titanium ions [27]. The dissociation equation of H_2O_2 in the aqueous solution brings peroxide ion O_2^{2-} and OH ligands, which facilitates the binuclear peroxotitanium complex slowly condensing to polynuclear complex $[(Ti_2O_5)(OH)_2]^0$. After hydrothermal treatment, the peroxotitanium complex exists as a monomer $[Ti(OH)_4(OH_2)_2]^0$ growing units by decomposing peroxo groups [28]. The octahedral $[Ti(OH)_4(OH_2)_2]^0$ units are favorable to link together by sharing edges leading to anatase formation [27].

Generally, the concentration of HCl is an important factor for control of the crystal structure [29]. During the crystallization process in our work, the acidic condition enhanced the Cl^- anion attack of the $[Ti(OH)_4(OH_2)_2]^0$ units, promoting the formation of the complex $[Ti(OH)_2Cl_2(OH_2)_2]^0$. The $[Ti(OH)_2Cl_2(OH_2)_2]^0$ units can joined together by sharing both edges and corners along the apical direction or the equatorial plane between the anatase and rutile phase, leading to the brookite phase [30]. The more Cl^- ions exist, the more octahedral $[Ti(OH)_2Cl_2(OH_2)_2]^0$ form, which leads to the generation of the brookite phase (as seen in sample TiH1 and TiH3). Moreover, the high acidic media (sample TiH10 and TiH16) with high excess of Cl^- ions eliminated a hydroxo ligand and then formed a $[Ti(OH)Cl_3(OH_2)_2]^0$ complex. That provided a weak barrier against the deoxolation process and effectively favors the corner-shared bonding along the [001] direction by the dehydration of OH ligand, yielding rutile [30, 31].

In our work, the growth of different phases TiO_2 could be formulated as the following equations:

$$Ti(SO_4)_2 + NH_4OH \rightarrow Ti(OH)_4 \downarrow + (NH_4)_2SO_4, \tag{2}$$

$$Ti(OH)_4 + H_2O_2 \rightarrow [(Ti_2O_5)(OH_2)_2]^0, \tag{3}$$

$$[(Ti_2O_5)(OH_2)_2]^0 + 7H_2O \rightarrow 2[Ti(OH)_4(OH_2)_2]^0 + O_2, \tag{4}$$

$$[Ti(OH)_4(OH_2)_2]^0 \xrightarrow{\text{hydrothermal}} TiO_2(\text{anatase}), \tag{5}$$

$$[Ti(OH)_4(OH_2)_2]^0 + 2HCl \rightarrow [Ti(OH)_2Cl_2(OH_2)_2]^0, \tag{6}$$

$$[Ti(OH)_2Cl_2(OH_2)_2]^0 \xrightarrow{\text{hydrothermal}} TiO_2(\text{brookite}), \tag{7}$$

$$[Ti(OH)_4(OH_2)_2]^0 + 3HCl \rightarrow [Ti(OH)Cl_3(OH_2)_2]^0, \tag{8}$$

$$[Ti(OH)Cl_3(OH_2)_2]^0 \xrightarrow{\text{hydrothermal}} TiO_2(\text{rutile}). \tag{9}$$

Several works reported the same growth mechanism for the growth of rutile phase induced by chloride anions [18]. However, an interesting phenomenon observed in this work is that the anatase phase is predominantly formed under high acidic conditions. The titanium precursor PTC used in our work is more stable (the zeta potential value of the PTC sol is −54.9 mV), which can weaken the interaction with Cl^- ions, and then protect the anatase phase. This deduction is supported by the

fact, that the unavailing formation of PTC precursor lead to a very low content of anatase phase of as-prepared TiO_2 samples, if simultaneously adding the H_2O_2 and HCl (as seen in Fig. S1). Thus, the high stability of PTC precursor provides a large window for adjustment of the crystal phase.

The morphology of TiO_2 nanocrystals samples prepared by different HCl/PTC ratios were characterized by TEM (Fig. 3). Sample TiH0 shows an irregular shape and the particle size is about 15.4 nm. Samples TiH1 and TiH3 display the similar shape and have a particle size of 14.2 and 19.7 nm, respectively. From the HRTEM micrograph (Fig. 3f), it can be observed that sample TiH3 had two lattice spaces 0.353 and 0.249 nm, which can be identified as the (101) face of anatase and the (014) plane of brookite, respectively [17]. Further increase of the HCl/PTC ratio led to the coexistence of nanorod and nanoparticles in the samples of TiH10 and TiH16 (Fig. 3d, e). The nanorod size for samples TiH10 and TiH16 are 94.0 and 253.6 nm for length, 24.3 and 66.3 nm for diameter, respectively. The nanoparticles size for samples TiH10 and TiH16 is 22.1 and 25.6 nm, respectively. Considering the HRTEM analysis (Fig. 3f, g), the nanorods are evidenced to be the rutile phase by the observation of the lattice space 0.329 nm, which are consistence with the (110) plane of rutile crystal structure [31]. Additional, the small nanoparticles adhering to the tip of the rutile nanorod, which was identified as the anatase and brookite phase by the existence of the (101) face of anatase and the (121) plane of the brookite phase. Briefly, the varied morphology of particles and enhanced particles size can be observed by increasing the HCl/PTC ratio.

The Brunauer–Emmett–Teller (BET) surface area of TiO_2 nanocrystals samples prepared by different HCl/PTC ratios is shown in Table 1. It was found that S_{BET} values of samples TiH0, TiH1, and TiH3 increased from 107.6 to 147.6 m^2/g, which
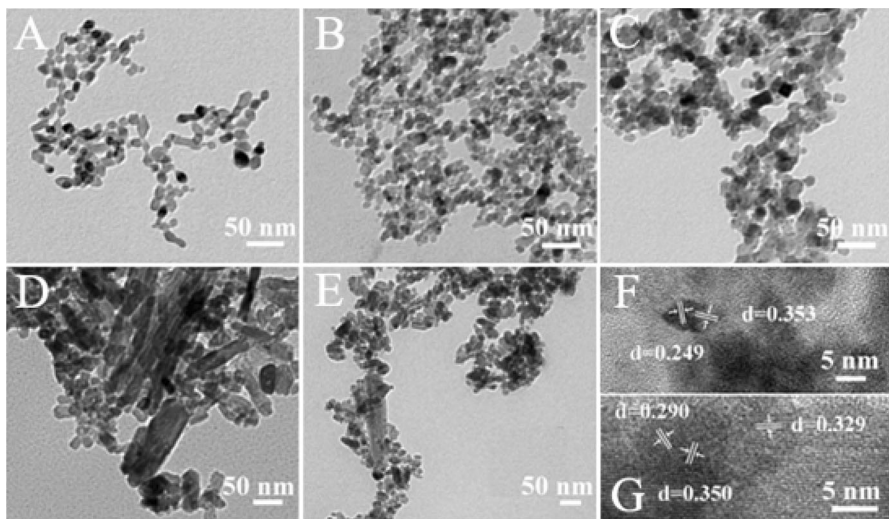
Fig. 3 TEM images of the TiO_2 nanocrystals prepared by different HCl/Ti molar ratios. a TiH0, b TiH1, c TiH3, d TiH10, e TiH16, f HRTEM image of TiH3 and g HRTEM image of TiH16

showed a high surface-to-volume ratio. However, the S_{BET} values of samples TiH10 and TiH16 is only 45.1 and 65.7 m^2/g, respectively. The large decrease in BET surface area for triphase coexistence TiO$_2$ samples can be attributed to the reduced particle size.

Figure 4 shows the diffuse reflectance spectra of TiO$_2$ nanocrystals samples prepared by different HCl/PTC ratios. The optical band gap energy satisfies the following equation for a crystalline semiconductor.

$$\alpha = \frac{K(hv - E_g)^{n/2}}{hv},$$ (10)

where α and E_g are absorption coefficients and band gap, K, is a constant, and hv is the photon energy. The value of n is equal to 1 for a direct transition [32]. The band gap of as-prepared TiO$_2$ nanocrystals samples can be calculated by the intercept of the tangent to the plot and listed in Table 1. It can be shown that sample TiH0 with pure anatase phase exhibits a band gap energy value of 3.24 eV, consistent with reported literature data [1]. As compared to the pure anatase phase, the biphase TiO$_2$ samples (TiH1 and TiH3) exhibited a slightly red shift, the E_g value decreased to 3.13 and 3.12 eV for samples TiH1 and TiH3, respectively. The results can be attributed to the effect of the brookite phase, since the energy gap of brookite TiO$_2$ is 3.11 eV [27]. The triphase coexistence TiO$_2$ samples show a red shift compared to biphase TiO$_2$ samples. The E_g of samples TiH10 and TiH16 is 3.12 and 3.0 eV, respectively. This change is due to the appearance of rutile phase, since the E_g of rutile TiO$_2$ is 2.8 eV [18].
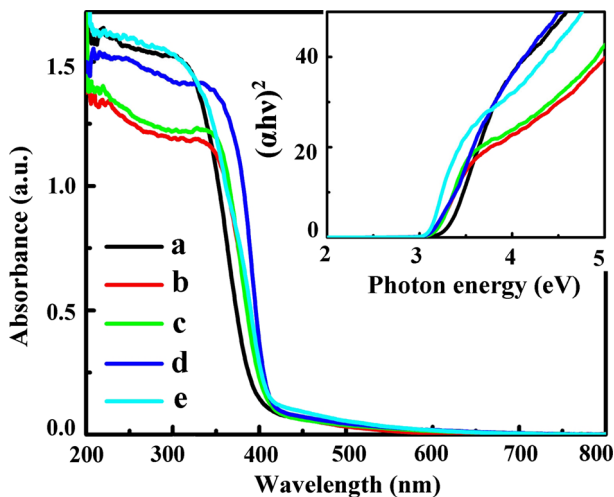

Fig. 4 Diffuse reflectance spectra of the TiO$_2$ nanocrystals prepared by different HCl/PTC ratios. The *inset* shows the plot of $(\alpha hv)^{1/2}$ as a function of the photon energy for as-prepared samples. *a* TiH0, *b* TiH1, *c* TiH3, *d* TiH10, *e* TiH16

Photocatalytic activities and mechanism of mixed phase TiO$_2$ nanocrystals

The photocatalytic degradation corresponds to a pseudo-first-order reaction as shown in Fig. 5a. The reaction can be expressed by $Ln(C_0/C) = kt$, where C_0 is the original reaction concentration of phenol (mg/L), C is the concentration (mg/L) at a given time (h) and k is the apparent reaction rate constant (h^{-1}). Half-life $t_{1/2}$ (h) is assumed to calculated from k by $t_{1/2} = Ln2/k$ [33]. The degradation rate, k and $t_{1/2}$ are calculated and shown in Table 2. The k is 0.2081, 0.3646, 0.9061, 0.0506, and 0.0792 for sample TiH0, TiH1, TiH3, TiH10, and TiH16, respectively. The sample TiH3 exhibits the highest photocatalytic activity.

Moreover, the biphase anatase/brookite samples (TiH1, TiH3) show a higher photodegradation rate than that of the pure anatase sample (TiH0). The photocatalytic activity is affected by many factors, including crystal phase structure, crystallite size, specific surface area, preparation method, and so on. In order to find the main factors, we normalized the k (h^{-1}) constant with the specific surface areas, and they are listed in Table 2. After normalizing, the apparent reaction rate constant of sample TiH3 still is 3.4 times higher than that of TiH0. Generally, the photoluminescence emission spectra have been widely used to evaluate the efficiency of charge carrier trapping, immigration, and transfer, and also to understand the recombination rate of electron–hole pairs [24]. The fluorescence emitted by as-prepared samples in our study was also observed and shown in Fig. 6. From the spectral lines, it was clearly observed that the PL spectrum of the biphase anatase/brookite TiO$_2$ sample was of much lower intensity than that of the pure anatase TiO$_2$ sample, which may be attributed to the mixed phase TiO$_2$ slowing the radiative recombination process [12]. Hence, this enhanced photocatalytic activity
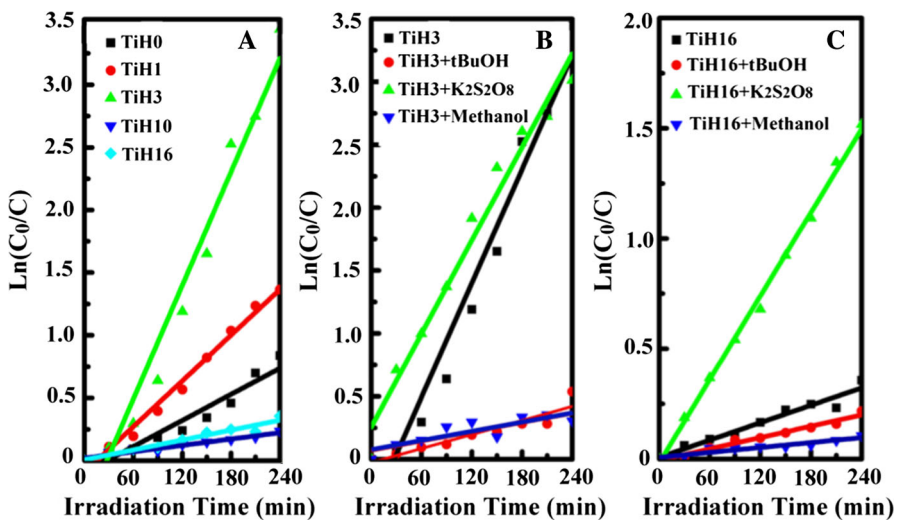
Fig. 5 Linear transform $Ln(C_0/C) = kt$ of the kinetic curves of phenol degradation. **a** TiO$_2$ samples prepared by different HCl/Ti molar ratios; **b** TiH3 (biphase TiO$_2$) with different scavengers; **c** TiH16 (triphase TiO$_2$) with different scavengers

Table 2 Photodegradation of phenol on different samples

Sample	Degradation of phenol (%)	Apparent rate constant k (h^{-1})	Normalized rate constant k (h^{-1})	Half-life $t_{1/2}$ (h)
TiH0	56.8	0.2081	0.0019	3.3
TiH1	74.5	0.3646	0.0025	1.9
TiH3	96.8	0.9061	0.0065	0.8
TiH3 + tBuOH	41.5	0.1116	–	6.2
TiH3 + K$_2$S$_2$O$_8$	95.1	0.7422	–	0.9
TiH3 + methanol	26.2	0.0738	–	9.4
TiH10	21.0	0.0506	0.0011	13.7
TiH16	30.0	0.0792	0.0012	11.8
TiH16 + tBuOH	19.6	0.0514	–	13.5
TiH16 + K$_2$S$_2$O$_8$	78.0	0.3792	–	1.8
TiH16 + methanol	10.0	0.0224	–	31.0

Fig. 6 Photoluminescence spectra of the TiO₂ nanocrystals prepared by different HCl/Ti molar ratios
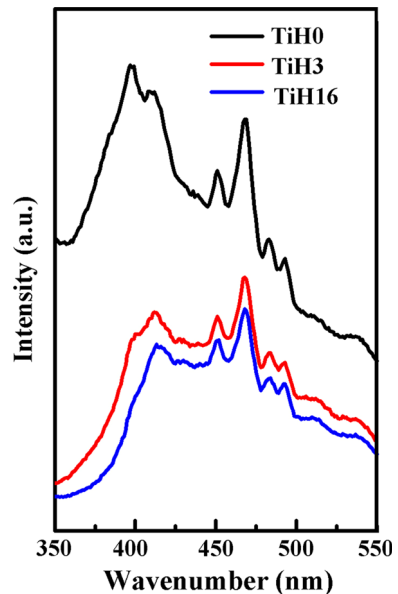
of sample TiH3 is mainly attributed to the biphase crystal structure, which can effectively separate photo-induced electron–hole pairs [34].

Evidently, the heterojunction structure plays a vital role in the enhancement of photocatalytic activity. It could be presumed that the matching multi-heterojunction structure shows better charge separation ability, since the greater is the energetic difference between the bands , the greater the driving force of the photogenerated

charge becomes [35]. In this work, the sample TiH16 with anatase/brookite/rutile triphase TiO_2 showed the lowest PL intensity (Fig. 6), which indicated that this was the best effective charge separation performance. However, the photocatalytic performance of anatase/brookite/rutile triphase TiO_2 samples (TiH10, TiH16) are lower than that of single anatase (TiH0) and anatase/brookite biphase TiO_2 samples (TiH1, TiH3), as seen in Fig. 5a and Table 2. The different results may indicate that the photocatalytic process for biphase and triphase coexistence TiO_2 occurs through a different mechanism.

In order to elucidate the photocatalytic mechanism of biphase and triphase coexistence TiO_2 photocatalysts, the influence of photogenerated holes scavenge (methanol), ·OH radical scavenge (t-BuOH), and photogenerated electrons scavenge ($K_2S_2O_8$) on the degradation of phenol were investigated for samples TiH3 and TiH16 (as seen in Fig. 5b, c; Table 2) [36].

For the biphase TiO_2 sample (TiH3), the adding of $K_2S_2O_8$ had almost no observable effect on the conversion rate of phenol. However, the degradation rates of phenol were significantly reduced by adding both t-BuOH and methanol. Accordingly, the photocatalytic degradation of phenol for biphase TiO_2 samples is caused by the action of h_{vb}^+ and/or ·OH radical, although the phenolic compounds can direct oxidation via h_{vb}^+ [37]. The primary fate of h_{vb}^+ in this experiment was mainly to generate the ·OH radical, since the influence degree of ·OH radical is $(k_{(TiH3)} - k_{(TiH3-tBuOH)})/k_{(TiH3)} \times 100\ \% = 87.7\ \%$, while the influence degree of h_{vb}^+ is $(k_{(TiH3)} - k_{(TiH3-t+\ methanol)})/k_{(TiH3)} \times 100\ \% = 91.9\ \%$. Thus, the ·OH radical generated from the h_{vb}^+ was responsible for the degradation of phenol for the biphase system. Regarding the triphase TiO_2 sample (TiH16), the photocatalytic degradation of phenol was deeply inhibited with the addition of methanol. However, the adding of t-BuOH had less influence on the degradation rate of phenol, implying that h_{vb}^+ instead of ·OH radical had a crucial role in the process of phenol oxidation. Furthermore, the presence of $K_2S_2O_8$ in TiH16 suspensions promoted greatly the degradation rate (almost 2.6 times), revealing that the $S_2O_8^{-2}$ can trap e_{cb}^- to leave more h_{vb}^+ available for photocatalytic reaction [38].

Obviously, the difference in photocatalytic rate for biphase and triphase TiO_2 samples is due to a different mechanism. The sample TiH3 with anatase/brookite biphase exhibits higher photocatalytic activity than that of sample TiH1. As in previous analysis, the enhanced photocatalytic activity mainly should be attributed to the heterophase junction structure.

For anatase/brookite/rutile triphase coexistence TiO_2 samples (TiH16), the valence band top is higher than that of anatase/brookite biphase sample [39, 40], which limited the h_{vb}^+ available for the generation of ·OH radical. The photocatalytic process for triphase coexistence TiO_2 sample is that h_{vb}^+ directly reacts with phenol. From the PL results, the separating ability of photogenerated charges is the highest for the triphase coexistence TiO_2 samples. However, the photogenerated h_{vb}^+ in triphase coexistence TiO_2 samples cannot transfer effectively to the surface –OH group and form the ·OH radical with higher redox ability [35], which was inclined to the recombination of separated charges. Therefore, the triphase coexistence TiO_2 samples in this work show lower photocatalytic activity compared with pure anatase and anatase/brookite biphase TiO_2 samples. The enhanced degradation rate by
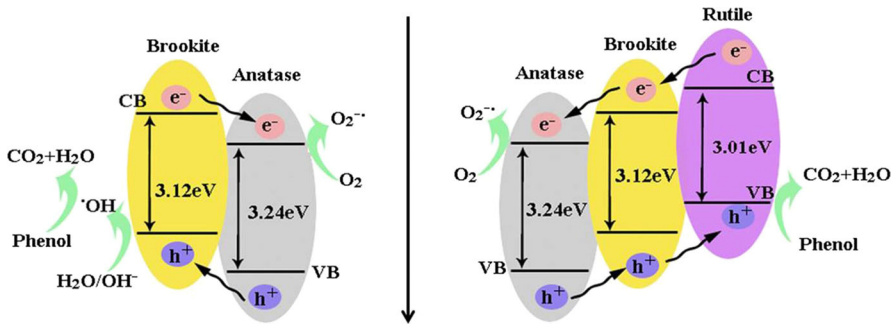
Fig. 7 Scheme of the photocatalytic mechanism of mixed phase TiO$_2$ nanocrystals

adding the photogenerated electrons scavenge proved this deduction very well. Based on the above analysis, the matched redox energy levels between photocatalyst and surface activated group are the key factor for the photocatalytic mechanism (as shown in Fig. 7).

Therefore, the design of a heterojunction photocatalyst system must consider not only the suitable energy band structure of heterojunction photocatalyst for effective separating of photogenerated charges, but also the matching redox energy levels between photocatalyst and their surface group for forming the activated radical such as $\cdot$OH, $O_2^{-\cdot}$ and $HO_2^{\cdot}$ radical, etc.

Conclusion

The mixed-phase TiO$_2$ nanocrystals with tunable phase composition have been successfully synthesized by a simple hydrothermal method. By changing the HCl/PTC ratio, the ratio of anatase to anatase/brookite biphase and anatase/brookite biphase to anatase/rutile/brookite triphase were easily tuned. The change in the acidity and chlorine anions content of the precursor solutions is the key factor for tuning of phase compositions. Additionally, the anatase phase is predominantly formed in the triphase or biphase TiO$_2$ nanocrystals samples under high acidic condition due to the high stability of the PTC precursor. The photocatalytic measurement results show that the photocatalytic activity is anatase/brookite biphase > anatase monophase > anatase/rutile/brookite triphase TiO$_2$ nanocrystals. Sample TiH3, which is composed of 65.2 % anatase and 34.8 % brookite, shows the highest photocatalytic activity. Although the anatase/rutile/brookite triphase TiO$_2$ nanocrystals samples show the most effective separation ability of photo-induced electron–hole pairs, the anatase/brookite biphase TiO$_2$ nanocrystals samples exhibit the highest photocatalytic activity, which can be attributed to effectively forming the active radicals. Thus, the design of a heterojunction photocatalyst must consider not only the suitable the energy band structure for effective separating of photogenerated charges, but also matching the energy level between heterojunction photocatalysts and their surface group for forming the active radical.

References

1. A. Hegazy, E. Prouzet, Chem. Mater. **24**, 245 (2012)
2. Z. Sun, J.H. Kim, Y. Zhao, F. Bijarbooneh, V. Malgras, Y. Lee, Y.-M. Kang, S.X. Dou, J. Am. Chem. Soc. **133**, 19314 (2011)
3. J. Xu, W. Wang, S. Sun, L. Wang, Appl. Catal. B Environ. **111**, 126 (2012)
4. J. Su, L. Guo, N. Bao, C.A. Grimes, Nano Lett. **11**, 192 (2011)
5. Y. Zhou, K.A. Fichthorn, J. Phys. Chem. C **116**, 8314 (2012)
6. H. Wang, X. Gao, G. Duan, X. Yang, X. Liu, J. Environ. Chem. Eng. **3**, 603 (2015)
7. J.-L. Mi, C. Clausen, M. Bremholm, N. Lock, K.M.Ø. Jensen, M. Christensen, B.B. Iversen, Cryst. Growth Des. **12**, 6092 (2012)
8. M.-C. Wu, P.-H. Lee, D.-L. Lee, Int. J. Hydrogen Energy **40**, 4558 (2015)
9. B.K. Mutuma, G.N. Shao, W.D. Kim, H.T. Kim, J. Colloid Interface Sci. **442**, 1 (2015)
10. A.A. Vargeese, K. Muralidharan, Mater. Chem. Phys. **139**, 537 (2013)
11. L. Gai, X. Duan, H. Jiang, Q. Mei, G. Zhou, Y. Tian, H. Liu, CrystEngComm **14**, 7662 (2012)
12. R. Boppella, P. Basak, S.V. Manorama, ACS Appl. Mater. Interfaces **4**, 1239 (2012)
13. Y.L. Liao, W.X. Que, Q.Y. Jia, Y.C. He, J. Zhang, P. Zhong, J. Mater. Chem. **22**, 7937 (2012)
14. J. Zhang, X. Xiao, J. Nan, J. Hazard. Mater. **176**, 617 (2010)
15. Y. Hou, X. Li, Q. Zhao, G. Chen, C.L. Raston, Environ. Sci. Technol. **46**, 4042 (2012)
16. Z. Wu, G. Zhao, Y.-N. Zhang, H. Tian, D. Li, J. Phys. Chem. C **116**, 12829 (2012)
17. C. Perego, Y.-H. Wang, O. Durupthy, S. Cassaignon, R. Revel, J.-P. Jolivet, ACS. Appl. Mater. Interfaces **4**, 752 (2012)
18. J.G. Li, T. Ishigaki, X.D. Sun, J. Phys. Chem. C **111**, 4969 (2007)
19. N. Murakami, T.-A. Kamai, T. Tsubota, T. Ohno, CrystEngComm **12**, 532 (2010)
20. Y. Liu, H. Wang, Y. Wang, H. Xu, M. Li, H. Shen, Chem. Commun. (Camb) **47**, 3790 (2011)
21. D.H. Wang, L. Jia, X.L. Wu, L.Q. Lu, A.W. Xu, Nanoscale **4**, 576 (2012)
22. H. Thakur, R. Kumar, P. Thakur, N.B. Brookes, K.K. Sharma, A.P. Singh, Y. Kumar, S. Gautam, K.H. Chae, J. Appl. Phys. **110**, 083718 (2011)
23. S.I. Seok, M. Vithal, J.A. Chang, J. Colloid Interface Sci. **346**, 66 (2010)
24. Y. Zhao, J. Liu, L. Shi, S. Yuan, J. Fang, Z. Wang, M. Zhang, Appl. Catal. B Environ. **103**, 436 (2011)
25. Y. Zhao, J. Liu, L. Shi, S. Yuan, J. Fang, Z. Wang, M. Zhang, Appl. Catal. B Environ. **100**, 68 (2010)
26. J. Liu, Y. Zhao, L. Shi, S. Yuan, J. Fang, Z. Wang, M. Zhang, ACS. Appl. Mater. Interfaces **3**, 1261 (2011)
27. J.F. Zhi, Y. Zhang, L.Z. Wu, Q.H. Zeng, J. Phys. Chem. C **112**, 16457 (2008)
28. M. Nag, S. Ghosh, R.K. Rana, S.V. Manorama, J. Phys. Chem. Lett. **1**, 2881 (2010)
29. P. Sipos, Z. Ambrus, K. Mogyorosi, A. Szalai, T. Alapi, K. Demeter, A. Dombi, Appl. Catal. A Gen. **340**, 153 (2008)
30. A. Pottier, C. Chanéac, E. Tronc, L. Mazerolles, J.P. Jolivet, J. Mater. Chem. **11**, 1116 (2001)
31. H. Zhang, X. Liu, Y. Li, Q. Sun, Y. Wang, B.J. Wood, P. Liu, D. Yang, H. Zhao, J. Mater. Chem. **22**, 2465 (2012)
32. H.K. Jong, S. Kim, A.J. Bard, Nano Lett. **6**, 24 (2006)
33. L. Ge, J. Liu, Appl. Catal. B Environ. **105**, 289 (2011)
34. A.A. Vargeese, K. Muralidharan, J. Hazard. Mater. **192**, 1314 (2011)
35. S. Song, F. Hong, Z. He, Q. Cai, J. Chen, J. Colloid Interface Sci. **378**, 159 (2012)
36. L. Gu, J. Wang, H. Cheng, Y. Zhao, L. Liu, X. Han, ACS. Appl. Mater. Interfaces **5**, 3085 (2013)
37. S.G. Kumar, L.G. Devi, J. Phys. Chem. A **115**, 13211 (2011)
38. A. Adhikary, A. Kumar, J. Am. Chem. Soc. **135**, 3121 (2013)
39. F. Xu, W. Xiao, B. Cheng, J. Yu, Int. J. Hydrogen Energy **39**, 15394 (2014)
40. T. Ishigaki, J.G. Li, X.D. Sun, J. Phys. Chem. C **111**, 4969 (2007)